Journal of The Electrochemical Society, 2021 **168** 024502

The Impact of Antimony on the Performance of Antimony Doped Tin Oxide Supported Platinum for the Oxygen Reduction Reaction

Daniel Jalalpoor,[1] Daniel Göhl,[2] Paul Paciok,[3] Marc Heggen,[3] Johannes Knossalla,[1] Ivan Radev,[4] Volker Peinecke,[4] Claudia Weidenthaler,[1] Karl J. J. Mayrhofer,[2,5,*] Marc Ledendecker,[2,6,z] and Ferdi Schüth[1,z]

[1]*Department of Heterogeneous Catalysis, Max-Planck-Institut für Kohlenforschung, 45470 Mülheim an der Ruhr, Germany*
[2]*Department of Interface Chemistry and Surface Engineering, Max-Planck-Institut für Eisenforschung GmbH, 40237 Düsseldorf, Germany*
[3]*Ernst Ruska-Centre for Microscopy and Spectroscopy with Electrons and Peter Grünberg Institute, Forschungszentrum Jülich GmbH, 52425 Jülich, Germany*
[4]*The Hydrogen and Fuel Cell Center (ZBT GmbH), 47057 Duisburg, Germany*
[5]*Forschungszentrum Jülich GmbH, Helmholtz Institute Erlangen-Nürnberg for Renewable Energy (IEK-11), 91058 Erlangen, Germany*
[6]*Department of Technical Chemistry, Technical University Darmstadt, 64287 Darmstadt, Germany*

Antimony doped tin oxide (ATO) supported platinum nanoparticles are considered a more stable replacement for conventional carbon supported platinum materials for the oxygen reduction reaction. However, the interplay of antimony, tin and platinum and its impact on the catalytic activity and durability has only received minor attention. This is partly due to difficulties in the preparation of morphology- and surface-area-controlled antimony-doped tin oxide materials. The presented study sheds light onto catalyst–support interaction on a fundamental level, specifically between platinum as a catalyst and ATO as a support material. By using a previously described hard-templating method, a series of morphology controlled ATO support materials for platinum nanoparticles with different antimony doping concentrations were prepared. Compositional and morphological changes before and during accelerated stress tests are monitored, and underlying principles of deactivation, dissolution and catalytic performance are elaborated. We demonstrate that mobilized antimony species and strong metal support interactions lead to Pt/Sb alloy formation as well as partially blocking of active sites. This has adverse consequences on the accessible platinum surface area, and affects negatively the catalytic performance of platinum. Operando time-resolved dissolution experiments uncover the potential boundary conditions at which antimony dissolution can be effectively suppressed and how platinum influences the dissolution behavior of the support.
 [DOI: 10.1149/1945-7111/abd830]

Manuscript submitted October 12, 2020; revised manuscript received December 8, 2020. Published February 2, 2021.

Supplementary material for this article is available online

Proton exchange membrane fuel cells (PEMFC) are the state of the art technology for mobile fuel cell applications.[1] Their performance is mainly controlled by the sluggish kinetics of the oxygen reduction reaction (ORR) taking place at the cathode.[2] The acidic and electrooxidative conditions inside the PEMFC, however, pose substantial challenges to the materials employed. For enhanced noble metal utilization, nanoparticles with a high surface to volume ratio are usually supported on high surface area supports. Carbon is by far the most used support material.[3] Nevertheless, the activity loss caused by carbon corrosion and platinum dissolution, especially at high electrode potentials and high temperatures, remains significant, raising interest in alternative support materials.[4–6] Due to the harsh conditions in PEMFCs, the number of possible material candidates is limited and mostly oxides, nitrides and carbides are proposed to be sufficiently conductive and stable.[7–9] Antimony doped tin oxides meet these requirements and tolerate catalyst poisons such as CO to a higher extent compared to Pt/C.[10–14] The properties of ATO with various antimony contents and morphologies were examined in several publications for ATO aerogels,[15,16] nanoparticles,[17–19] fibers,[20] and films[21] (cf. Table SI available online at stacks.iop.org/JES/168/024502/mmedia for a selection of recent publications). However, the effect of different antimony doping levels on the catalyst performance and durability remains largely unexplored. From the publications mentioned, two general trends can be deduced: firstly, the specific activity of ATO supported catalysts is lower than that of carbon-supported platinum at comparable electrochemical surface areas (ECSA) and support particle sizes (cf. Table SI and[22]). Secondly, the ECSA decays to a lower extent throughout accelerated stress tests in comparison to the surface areas of carbon supported platinum catalysts. However, the specific activity after accelerated stress tests is only addressed in few reports,[15,19,23] and the impact of the support material on the catalyst's activity and possible deactivation mechanisms remains largely unknown.

In this work, the interaction of platinum nanoparticles with antimony tin oxide supports was examined in detail, and the implication of antimony concentration on the electrochemical performance was elaborated. A recently reported, versatile hard-templating synthesis method was used to obtain ATO materials with similar morphologies at different and controllable antimony doping concentrations.[24] Specifically, surface sensitive techniques such as X-ray photoelectron spectroscopy (XPS) were combined with X-ray diffraction (XRD) and transmission electron microscopy (TEM) paired with energy dispersive X-ray spectroscopy (EDX) to uncover the catalysts' morphology, crystal structure, the local element distribution and its surface characteristics. In-situ, time and potential controlled flow cell measurements were coupled to an inductively coupled plasma mass spectrometer (ICP-MS) to identify possible degradation mechanisms. Identical location (scanning) TEM (IL-STEM) measurements were used to track changes in elemental distribution and the structure of individual particles after various degradation protocols. Altogether, our results present important insights on metal-support interactions between platinum and ATO and their impact on activity, performance, dissolution behavior and long-term stability.

Experimental

Synthesis.—For further details on the applied chemicals and the syntheses, please refer to the supporting information.

*Electrochemical Society Member.
[z]E-mail: marc.ledendecker@tu-darmstadt.de; schueth@kofo.mpg.de

ATO support.—The synthesis of the ATO support, by hard-templating from a silica template, is described in detail elsewhere ([25,24]). The support materials used here are equivalent to the introduced mesoporous ATO materials with different antimony dopant concentration (numbers 10, 11, 13, 15 and 16). Additionally, a pure SnO_2 material was prepared with the same synthesis method without addition of antimony. For details on the synthesis, please refer to the publication mentioned above and the supporting information.

Platinum loading.—For the one-pot synthesis, the platinum nanoparticles are formed by applying a polyol method in the presence of the respective support material. Typically, the support material (100 mg) is dispersed in ethylene glycol (21.5 ml) by ultrasonication (30 min). PVP (30.42 mg) and excess of K_2PtCl_4 (50 mg) is added and the dispersion is further sonicated (15 min). The dispersion is transferred into a preheated oil bath (150 °C) and stirred at constant temperature (30 min) under reflux. Afterwards, the mixture is removed from the oil bath, naturally cooled down to room temperature and stirred for further 16 h. The particles are collected by centrifugation (9000 rpm, 8700 x g, 10 min) washed twice with ethanol (40 ml) and dried for 24 h (80 °C).

An analogous procedure was used for the two-pot synthesis with the exception that the support materials were added after particle formation and only half the batch size was used. Therefore, the support material (50 mg) was dispersed in 3 ml ethylene glycol by sonication (30 min) and added to the preformed nanoparticles after cooling the reaction mixture to room temperature. The mixture was stirred at room temperature for 16 h before the particles were collected and washed as described before.

For the synthesis of platinum particles supported on the carbon hollow graphitic sphere support, please refer to a previous publication.[26]

Characterization methods.—TEM measurements were performed on a Hitachi H-7100 instrument (100 kV) and a Hitachi S-3500N Scanning Electron Microscope (SEM), equipped with a 5i (Li) Pentalet Plus Detector (Oxford Instruments GmbH) EDX Detector. SEMs were recorded using a spherical aberration corrected STEM/SEM HD-2700 (200 kV, Cold FEG) equipped with an EDX detector (EDAX OCTANE T Ultra W 200 mm^2 SDD, TEAM Software).

For identical location transmission electron microscopy, gold TEM finder grids (S147A9, Plano GmbH) were coated with an aqueous catalyst suspension (10 μl, 0.05 $g_{cat}{\cdot}l^{-1}$). After drying, the sample was examined in a Cs-corrected (CEOS GmbH), FEI Titan 80-200 ("ChemiSTEM") electron microscope equipped with a high angle annular dark field (HAADF) detector at 80 kV to minimize beam damage. "Z-contrast" conditions were achieved by using a probe semi-convergence angle of 24.7 mrad and an inner collection semi angle of 88.4 mrad. Elemental maps were recorded by EDX using four large-solid-angle symmetrical Si drift detectors. To prevent beam damage, the acquisition time for each elemental map was 5 min. After the characterization, the catalyst-covered TEM grid was used as a working electrode in electrochemical degradation experiments with a carbon rod as counter electrode. For the accelerated aging experiments, the potential was cycled between 0.4 and 1.0 V_{RHE} for 10,800 times with a potentiostat (SP 50, Bio-Logic Science Instruments) at 20 °C. The homemade three electrode glass cell was equipped with a RHE as reference electrode (Gaskatel, HydroFlex). Argon saturated perchloric acid (0.1 $mol{\cdot}l^{-1}$, Merck, suprapur) was used as electrolyte. The iR drop was measured and was corrected for by the current interrupt method. After the ASTs, the grid was dipped several times into ultrapure water to remove electrolyte residues. After drying, the grid was transferred to the electron microscope and the pre-characterized catalyst agglomerates were re-examined.

XRD data were recorded with a Debye–Scherrer transmission diffractometer (Stoe STADI P). The instrument was equipped with a primary Ge(111) monochromator (Mo-Kα_1 radiation). The samples were placed in borosilicate glass capillaries (diameter = 0.5 mm). The data were typically collected in the range of 5°–50° (2θ) with a step width of 0.015° and counting times adjusted to the sample requirements. For structure refinement, TOPAS5[27] was used. As starting crystal structures, the following sources were used: SnO_2[28] and Pt.[29] The atomic coordinates were fixed while the lattice parameters, scaling factors, and profile parameters were refined. Phase quantification is based on the Rietveld refinements.

XPS measurements of the Pt/ATO samples were carried out on a Quantera II (Physical Electronics, Chanhassen, MN, USA), applying a monochromatic Al Kα X-ray source (1486.6 eV) operating at 15 kV and 25 W. The C 1s signal at 284.0 eV was used to reference the binding energy scale. Analysis of the spectra has been carried out with the Casa XPS software. For powder measurements, the catalyst was deposited onto a conductive carbon tape, which was attached to a sputtered gold film.

N_2 sorption measurements to determine BET surface areas and pore volumes were carried out using a Micromeritics 3Flex device. The materials were activated at 250 °C for 6 h in vacuum. The measurements were performed at 77.4 K using a static volumetric method, and a relative pressure tolerance of 5% for the equilibration intervals. For relative pressures below 0.1 $p{\cdot}p_0^{-1}$, an incremental dose mode (15 $cm^3{\cdot}g^{-1}$ STP with 10 s equilibration intervals) was employed. The BET surface area was calculated from the adsorption branch in the range of 0.05 to 0.25 $p{\cdot}p_0^{-1}$. The Barrett, Joyner and Halenda (BJH) method was employed for the estimation of the pore size distribution from the desorption branch.

For RDE measurements, catalyst suspensions were prepared in 1 ml ultrapure water (Elga PURELAB® Plus, 18 MΩ·cm, TOC < 3 ppb). After ultrasonicaton, 20 μl of the suspension were drop casted onto the Glassy carbon (GC) electrode (d = 5 mm), so that the Pt loading was 20 $\mu g\ cm^{-2}$. Prior to deposition, the GC electrodes were polished with a slurry containing water and aluminum oxide (0.3 and 1 μm particle size). 0.1 M $HClO_4$ electrolyte was prepared from ultrapure water and 70% $HClO_4$ (Merck Suprapur®).

The measurements were performed at room temperature on a Gamry Reference 600 potentiostat with an in-house designed RDE setup. A three-compartment Teflon cell was used with a graphite rod counter electrode and a Ag/AgCl reference electrode (Metrohm, 3 M KCl) which was calibrated against a reversible hydrogen electrode (RHE) at the beginning of each measurement. All potentials are reported vs RHE. The reference electrode was separated by a Nafion® membrane (Tschurl modification) to avoid chloride contamination. Prior to measurements, the iR drop in the cell was determined by high frequency impedance.

The electrochemical active surface area (ECSA) was determined from CO-stripping and H_{UPD}, where the CV recorded directly after CO stripping served as background for the $ECSA_{CO}$ and vice versa. Conversion factors of 390 and 195 $\mu C{\cdot}cm^{-2}{}_{Pt}$ were used for CO stripping and H_{UPD} according to Ref. 30. The measurement consisted of 1) an activation protocol consisting of 200 cycles between 0.05 to 1.4 V at 200 mV s^{-1} in Ar-sat 0.1 M $HClO_4$. 2) The ORR activity was determined in O_2-sat electrolyte conducting cycles between 0.05 and 1.2 V at 50 mV s^{-1} and rotation speeds of 400, 900, 1600 and 2500 rpm. A CV in Ar-sat electrolyte served as background. The specific, normalized by the ECSA value as determined by H_{UPD}, and mass activities were determined from the CV recorded at 1600 rpm at 0.9 V for the anodic scan direction after the background was subtracted.

After activity determination, an accelerated stress test (AST) was performed, which consisted of 10800 cycles between 0.4 and 1.0 or 1.4 V at a scan rate of 1 $V{\cdot}s^{-1}$. After 0, 360, 1080, 2160, 3600, 5400, 7200, 10800 cycles the ECSA was determined with both CO stripping and H_{UPD}.

After the AST, the activity was again determined. For the samples where AST 1.0 V was conducted, a third activity determination was carried out after the second activity measurement and after electrolyte exchange of the used, antimony containing electrolyte against fresh 0.1 M $HClO_4$.

A scanning flow cell coupled to an inductively coupled plasma mass spectrometer (ICP-MS—NexION 300X, Perkin Elmer) was

used to perform the electrochemical/stability tests.[24,31,32] The measurements were conducted in 0.1 M $HClO_4$, prepared by diluting concentrated acid (Suprapur®, 70% $HClO_4$, Merck, Germany, in ultrapure water (PureLab Plus system, Elga, 18 MΩ cm, TOC < 3 ppb). A graphite rod was used as a counter electrode and an Ag/AgCl electrode (Metrohm, Germany) as reference. As an internal standard for tin and antimony ^{103}Rh and ^{130}Te were added directly before injection into the ICP-MS device. The standard flow rate was 180 $\mu l \cdot min^{-1}$ and the setup was calibrated daily.

For sample preparation, 2 mg of the samples were dispersed in NaOH solution (2 ml, 0.001 M) with addition of Nafion-solution (8 μl, 5 wt%, Sigma Aldrich) and after extended ultrasonic treatment, 0.5 μl were dropcasted on a glassy carbon plate. The resulting spots with a diameter of about 1.5 mm were measured as prepared by central location within the 2 mm SFC-cell opening positioned with the help of a vertical camera.

Results and Discussion

To systematically study the catalyst interaction with the support, ATO materials with antimony doping concentrations (calculated as (Sb/(Sb + Sn)) were prepared between 0 at% and 10 at% using a liquid salt melt templating method previously reported by our group.[24]

Critically, one challenge lies in the reported dependency of antimony doping on the overall ATO particle size distribution, which makes a fair comparison between materials difficult.[15,16] We set out to synthesize materials with similar morphology via hard templating. Thus, the influence of antimony on the catalytic performance of platinum can be studied independent from geometric parameters. For a legitimate comparison between carbon, the state-of-the-art fuel cell catalyst support, on the one hand and ATO on the other hand, hollow graphitic spheres (HGS) with similar morphologies were used as carbon reference material, prepared by a similar hard-templating method (Fig. S3).[22,26,33,34] The same silica hard-template was used for the synthesis of hollow spherical ATO materials, except for the 11% Sb-ATO sample, where mesoporous full spheres were prepared. Pt particle sizes, Pt loadings and surface area and pore sizes (determined through nitrogen sorption experiments) are comparable for all samples (cf. Table I). The 220 nm ATO spheres consist of interconnected ATO nanoparticles in the size range of 6 nm, the average pore diameter is 3–4 nm. As additional reference materials, hard-templated neat tin oxide (SnO_2) with similar morphology was synthesized and commercially available ATO nanoparticles were used (Sigma Aldrich). The latter has a surface area of 70 $m^2 \cdot g^{-1}$ with a broad ATO particle size distribution and a high antimony doping concentration of 15%. Relevant information on all materials can be found in Table I.

In a first series of experiments, platinum nanoparticles were formed at 150 °C in the presence of the ATO support using a polyol method to ensure homogeneous platinum distribution on the support —a one-pot synthesis approach. Exemplarily, the TEM micrographs and the corresponding elemental maps obtained via EDX of Pt-11% Sb-ATO are shown in Figs. 1a–1c. Spherical platinum nanoparticles in the range of 4 nm are homogeneously distributed over the ATO support material. The platinum nanoparticle size distribution corresponds well to that of the Pt-HGS reference material (Table I). For all antimony-containing samples prepared in a one-pot synthesis approach, antimony is enriched inside or on the periphery of the platinum nanoparticles (cf. Figs. 1b, 1c and Figs. S1 and S2). To date, at these low temperatures, a platinum antimony interaction has neither been observed nor discussed in the context of ATO supported platinum ORR catalysts.[19,35–37] The antimony species might either be deposited in the form of an oxide, facilitated by strong metal-support interactions, as adatoms on the platinum surface, or within the platinum framework, forming an alloy. To gain additional insight into the nature of the platinum–antimony interactions, XRD measurements were performed. The XRD measurement results of all

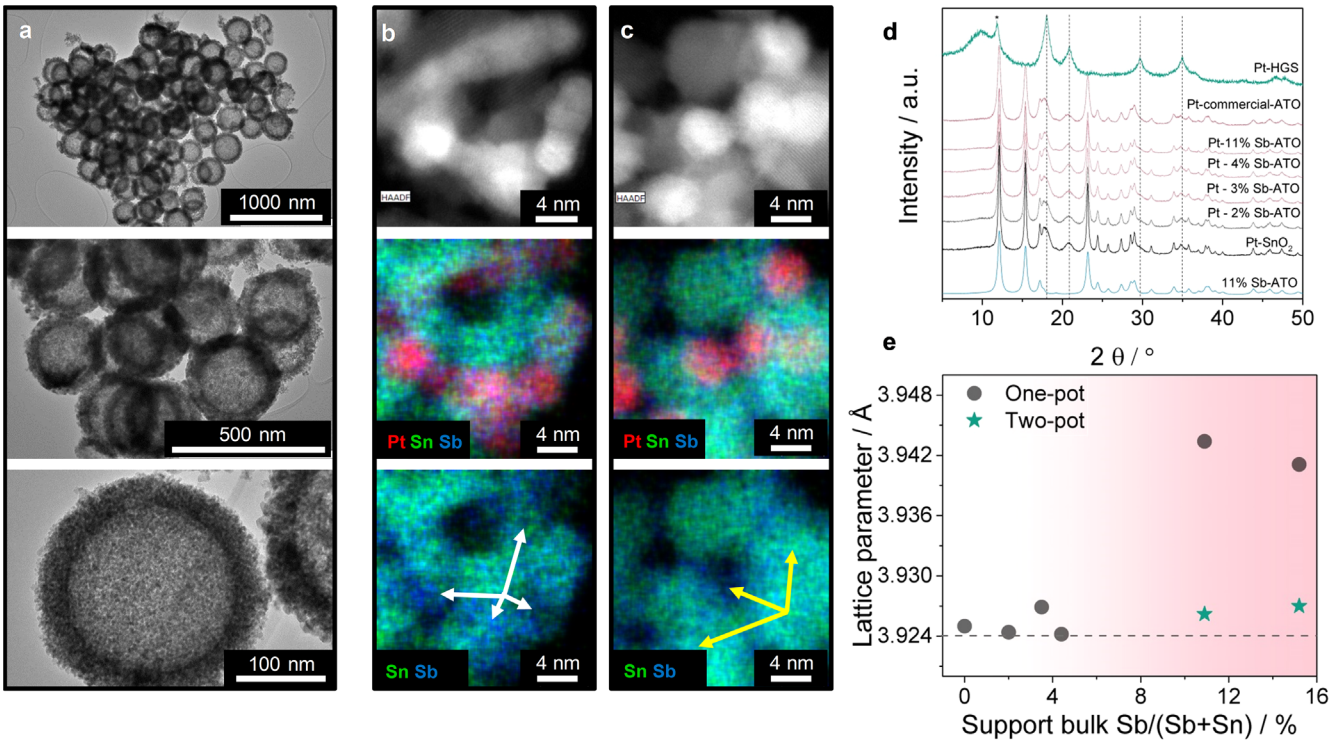

Figure 1. (a) Exemplary TEM images of the hollow spherical ATO support (11% Sb doping); TEM micrographs and the corresponding EDX element distribution exemplarily shown for (b) the one-pot Pt-11% Sb-ATO sample and for (c) the two-pot Pt-11% Sb-ATO sample; (d) XRD diffractograms of the different ATO supported platinum catalysts and the Pt-HGS reference. For comparison, a diffractogram of the 11% Sb-ATO support has been added. The dotted lines highlight the reflection positions of pure platinum. The asterisk corresponds to the reflection of the graphitized carbon. (e) Lattice parameters of platinum as determined by Rietveld refinement for the ATO supported one-pot samples (grey dots) and the two-pot samples (green stars). The diffraction of the platinum reference (taken from Ref. 38) is marked with a dotted line.

Table I. Properties of the prepared support materials. [1]Data given for support material.

Notation	Bulk Sb/ (Sb + Sn)[1]/%	XPS Sb/ (Sb + Sn)[1]/%	BET-surface area[1]/$m^2 \cdot g^{-1}$	Cond. impedance[1]/$S \cdot cm^{-1}$	Bulk Pt loading/wt%		XPS Pt loading/wt%	Pt part. size/nm
					Bulk-EDX	ICP-MS		
(Pt-) SnO2	0	0	85	$0.16 \cdot 10^{-3}$	18	—	—	4.0 ± 0.7
(Pt-) 2% Sb-ATO	2.0	3	105	$0.35 \cdot 10^{-3}$	20	18	23	3.8 ± 0.6
(Pt-) 3% Sb-ATO	3.5	5	115	$1.9 \cdot 10^{-3}$	18	18	19	3.8 ± 0.5
(Pt-) 4% Sb-ATO	4.4	6	100	$1.5 \cdot 10^{-3}$	19	18	20	4.3 ± 0.8
(Pt-) 11% Sb-ATO	10.9	13	125	$0.34 \cdot 10^{-3}$	14	14	20	3.9 ± 0.6
(Pt-) commercial-ATO	15.2	32	70	$3.2 \cdot 10^{-4}$	19	18	14	4.9 ± 0.8
(Pt-) HGS	—	—	1200	$5.6 \cdot 10^{-3}$	17	—	—	3.4 ± 0.6

ATO supported samples compiled in Fig. 1d are dominated by the reflections of the SnO_2 cassiterite structure of ATO. The broad reflections assigned to platinum correspond well to the small crystallite size. For Pt-11% Sb-ATO and commercial ATO, the reflections of platinum are shifted to lower angles. Further data analysis by Rietveld refinement (Fig. 1e) reveals indeed an increase in platinum lattice parameters at high antimony doping concentrations. The correlation between platinum lattice parameters and increasing antimony doping concentration, as well as the close, local proximity of antimony to platinum observed by EDX (Fig. 1b), strongly suggests the formation of a solid solution type face-centered cubic (fcc) Pt/Sb-alloy.

In order to further understand the impact of the applied synthesis conditions on the antimony-platinum interaction, a two-pot synthesis strategy was pursued (Pt-11% Sb ATO and Pt-commercial-ATO, 13 wt% and 7 wt% platinum loading, respectively, as determined by bulk-EDX). Here, platinum nanoparticles were synthesized separately and mixed at room temperature with the ATO support. The respective TEM micrographs and EDX maps are displayed in Fig. 1c. The one-pot and two-pot synthesis procedure resulted in similar particle size distributions and no change in morphology or structure could be observed. For the two-pot synthesis, the XRD-diffractograms give no indications of Pt/Sb-alloy formation and the platinum reflection positions match the expected reference values and the position for un-doped Pt-SnO_2. The antimony signal in the vicinity of platinum, as determined by EDX, is drastically reduced (ca. 25% to 11% average antimony mass concentration at platinum, cf. Fig. 4a, Figs. S1 and S2). The average antimony concentration in ATO is in accordance with the expected 6.6 wt% antimony doping concentration. For the one pot synthesis, we hypothesize that simultaneously to the chemically induced reduction of platinum, significant antimony amounts are dissolved and redeposited during the formation of platinum nanoparticles.[39] This is supported by literature where electrochemically induced reduction of antimony oxide leads to severe antimony dissolution.[24,40] Our findings suggest a strong affinity between platinum and antimony with potential implications for the overall catalytic performance.[41]

The interaction between platinum and antimony described above is expected to lead to altered electrochemical behavior. It could, for instance, manifest itself in the adsorption processes that are commonly used to determine the electrochemically active surface area (ECSA), or also in the electrochemical reaction itself. To test our hypothesis, the ECSA of pristine catalysts (beginning-of-life, BOL) was determined through the adsorption and subsequent oxidation of carbon monoxide (CO) and hydrogen underpotential deposition (H_{UPD}) as shown in Fig. 2a. The ECSAs of all oxide supported platinum catalysts are decreased in comparison to the carbon supported Pt reference (Pt/HGS). This is surprising as both, TEM and XRD measurements revealed particle/crystallite sizes similar to the Pt-HGS reference. We hypothesize that Pt/Sb alloy formation at high antimony concentrations, Sb-deposition or Sb-poisoning blocks active Pt-sites and results in lower CO and hydrogen accessibility.[15,19,42] This interaction might be irreversible.[43] The different ECSA values obtained for CO stripping and H_{UPD} (Fig. 2) could be one strong indication of Pt/Sb interaction as the reason for the reduced ECSA. The surface area determined by H_{UPD} is up to a factor of 1.5 higher compared to that obtained by CO stripping. The CO stripping cyclic voltammogram shows one broad CO oxidation peak at low potential and one sharp CO oxidation peak at higher potential when antimony is present. This finding might be rationalized by antimony adatoms suppressing the adsorption of CO as well as facilitating its oxidation by forming Sb–O(H) species with subsequently aided oxygen transfer.[12,14] For Pt-SnO_2, only a single, broad CO-stripping peak can be observed. This suggests that the adsorption and oxidation mechanism is altered in the presence of antimony.

Differences in the adsorption properties of platinum have been discussed before for e.g. Pt_3Ni and Pt_3Co and have been attributed to changes in the electronic structure.[44] The interactions appear not to

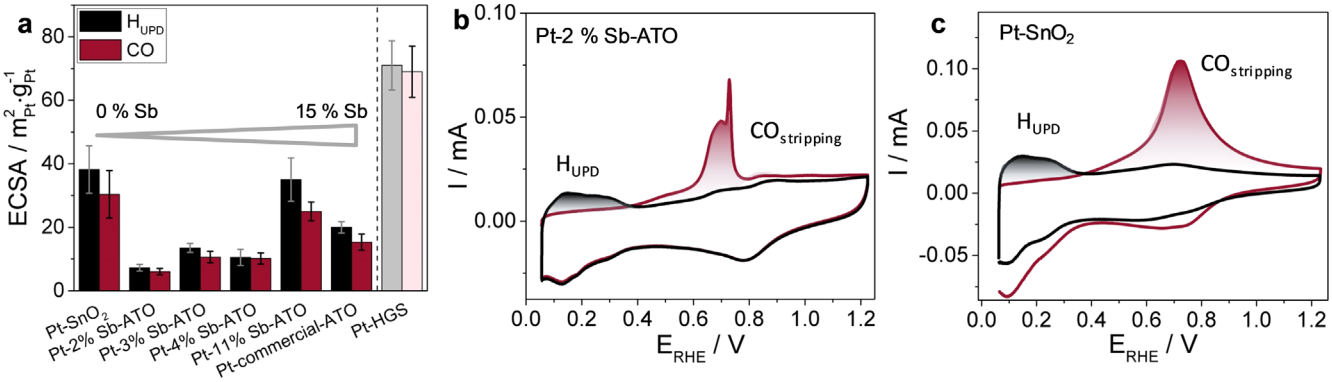

Figure 2. Platinum surface area determination. (a) Platinum ECSA values determined from H_{UPD} and CO-stripping. (b) CO-stripping and H_{UPD} determination of Pt-2% Sb-ATO. Areas used for determination of the surface areas are highlighted. (c) CO-stripping and H_{UPD} for the platinum supported on the antimony free SnO_2 support.

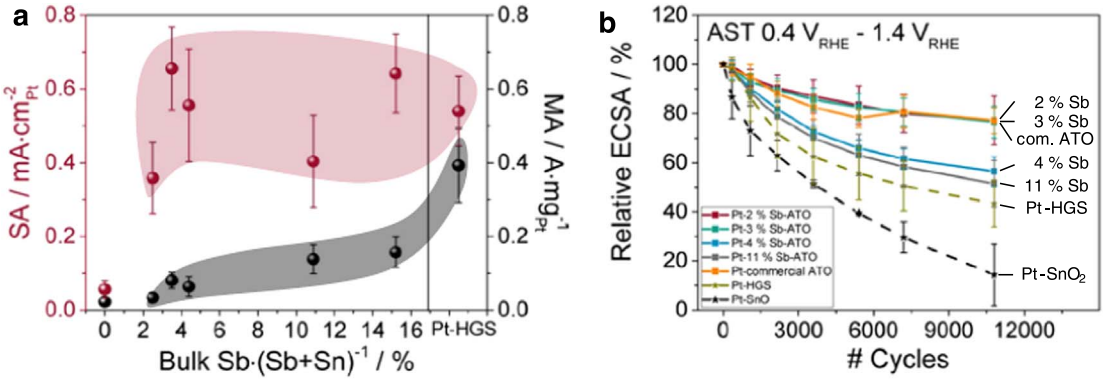

Figure 3. (a) Beginning-of-life specific and mass activities for the different ATO supported platinum catalysts as a function of antimony doping concentration. (b) Evolution of ECSA (H_{UPD}) values during the AST-1.4. ECSA values for the AST-1.0 are shown in the SI.

be trivial and the interested reader is referred to the SI for a more detailed discussion.

In order to test the hypothesis of platinum being poisoned and of surface blockage by antimony, the Pt-HGS reference was subjected to the used electrolyte of the Pt-4% Sb-ATO sample and the ECSA was compared (Fig. S10). While the H_{UPD} determined ECSA remains similar, a lower amount of CO is oxidized in the presence of antimony. The ECSA values obtained by both methods are still below the values determined for platinum supported on carbon, and it is unclear whether these values reflect the actual platinum surface area.[45] Geppert et al. found that covering TiO_2 does not influence the Pt H_{UPD} region but negatively influence the ORR, OER and HER activity.[46] Clearly, more work is required to find reliable methods for the analysis of surface species present and determination of surface area when oxide supports are used.

The ORR performance of all samples was tested and compared to Pt-HGS. Thin film rotating disk electrode (TF-RDE) measurements at 1,600 rpm in O_2−saturated 0.1 M $HClO_4$ were used to determine the ORR activity by decoupling the kinetic currents from mass limiting currents. The specific (SA) and the more application-relevant mass activities (MA) are displayed in Fig. 3a. The obtained beginning-of-life specific activities at 0.9 V_{RHE} for all ATO supported platinum nanoparticles are in accordance with Pt-HGS. Accessible platinum atoms possess a slightly lower but similar intrinsic activity in antimony containing catalysts compared to bare platinum on carbon. The SA for Pt on bare SnO_2 is drastically reduced. We assign the low activity of Pt/SnO_2 to the low conductivity (cf. Table I) that matches the broad CO oxidation peak during CO stripping and the reduced reduction peak of platinum oxide (cf. Fig. 2).

Due to the low ECSA of the antimony-containing samples, the MA is significantly reduced and matches published literature values for ATO supported platinum catalysts (cf. Table SI).

The long-term stability was determined by comparing the ECSA of the different Pt-ATO samples to Pt-HGS during accelerated stress tests (AST) consisting of 10,800 degradation cycles with two potential boundary conditions. To maintain high electron conductivity and to suppress major antimony mobilization, the potential was swept between a lower potential limit of 0.4 V_{RHE} and upper potential limits of 1.0 V_{RHE} (AST-1.0) and 1.4 V_{RHE} (AST-1.4). Upper potential limits between 1.0 V_{RHE} and 1.4 V_{RHE} can take place at open circuit potential, at fuel cell start up, or during fuel cell operation.[47,48] The ECSA development during ASTs reveals high stability at both, AST-1.0 and AST-1.4 in comparison to Pt-HGS (Figs. 3b and S8). The high stability in terms of ECSA might lead to concluding on an enhanced durability of Pt-ATO. The reasoning behind such a statement, however, seems too simplistic as the ECSA starting values differ strongly among each other. To shed more light onto the stability of platinum supported on ATO, the SA and MA was measured prior to and after the applied degradation protocols, revealing large activity losses of up to 80% during AST-1.4 (Fig. S7). This is interpreted to be caused by dynamic processes of antimony dissolution and re-deposition that occur e.g. during surface area determination and excursion to open circuit potential (OCP), as well as losses in conductivity due to antimony leaching from ATO. Potential excursions to OCP before and during testing play a crucial role due to a high amount of chemically dissolved antimony species (e.g. $Sb_2O_5 + 2H^+ \rightleftarrows 2SbO_2^+ + H_2O$; $Sb_2O_5 + H_2O \rightleftarrows 2SbO_3^- + 2H^+$)[40] that can redeposit during cycling. This hypothesis is supported by comparing the sample obtained from the one-pot synthesis to the sample from the two-pot synthesis (Fig. S11). The ECSA and SA after ASTs for both synthesis approaches are in a similar range, reflecting the high mobility of antimony during the electrochemical tests, which levels out the initial differences in platinum surface properties. We attributed the low specific activity of the Pt-SnO_2 sample, studied as the antimony-free endpoint of the series, to the low conductivity of the support.

In an additional testing series, the electrolyte was exchanged with fresh electrolyte (exchanged, EEX) after each AST-1.0 and the SA, MA and ECSA values were revised and compared to the initial values (Figs. S9 and S11). For all materials, the SA and MA decreases after degradation (AST-1.0) but re-increases after electrolyte exchange reaching or surpassing BOL values. A clear trend of Sb concentration on the SA could not explicitly be determined but the SA was, however, smaller compared to the Pt/HGS reference sample (cf. Fig. 3a). The differences between BOL and EOL-EEX were assigned also to other catalysts poisons such as Cl^- that can be still present even in non-adsorbing and ultrapure electrolytes such as $HClO_4$. We note that the electrochemical Teflon cell was boiled prior to the experiment in ultrapure water for 30 min, the reference electrode was a double junction Ag/AgCl electrode shielded by an additional Nafion® membrane to minimize the effect of chlorides from the reference electrode (cf. experimental results). On the one hand, our results highlight the necessity of post-degradation activity measurements to evaluate the performance in thin film rotating disk electrode analysis. On the other hand, we underline the significance of electrolyte exchange in EOL activity measurements, especially for support materials containing non-noble, dissolvable elements such as Sb.

To complement the understanding of antimony mobility and interaction with platinum during stability measurements, we followed the morphological and compositional evolution of individual catalyst particles prior to and after AST-1.0 and AST-1.4 by means of IL-STEM-EDX (Fig. 4). The local platinum, antimony and tin concentrations were determined by EDX mapping (ca. 4 nm^2 squares) both at positions with and without platinum. After AST-1.0, the materials proof to be morphologically stable and 40% of antimony dissolves when in close proximity to platinum while only 30% are removed from the ATO support where no platinum particles are located. This difference is probably caused by the loss of destabilized antimony species at/near platinum sites. Quantitative determination of the antimony concentrations before and after AST-1.0 are shown in Fig. 5b. The relative retention of Sb after AST-1.0 remains similar for all samples and the relative loss is neither

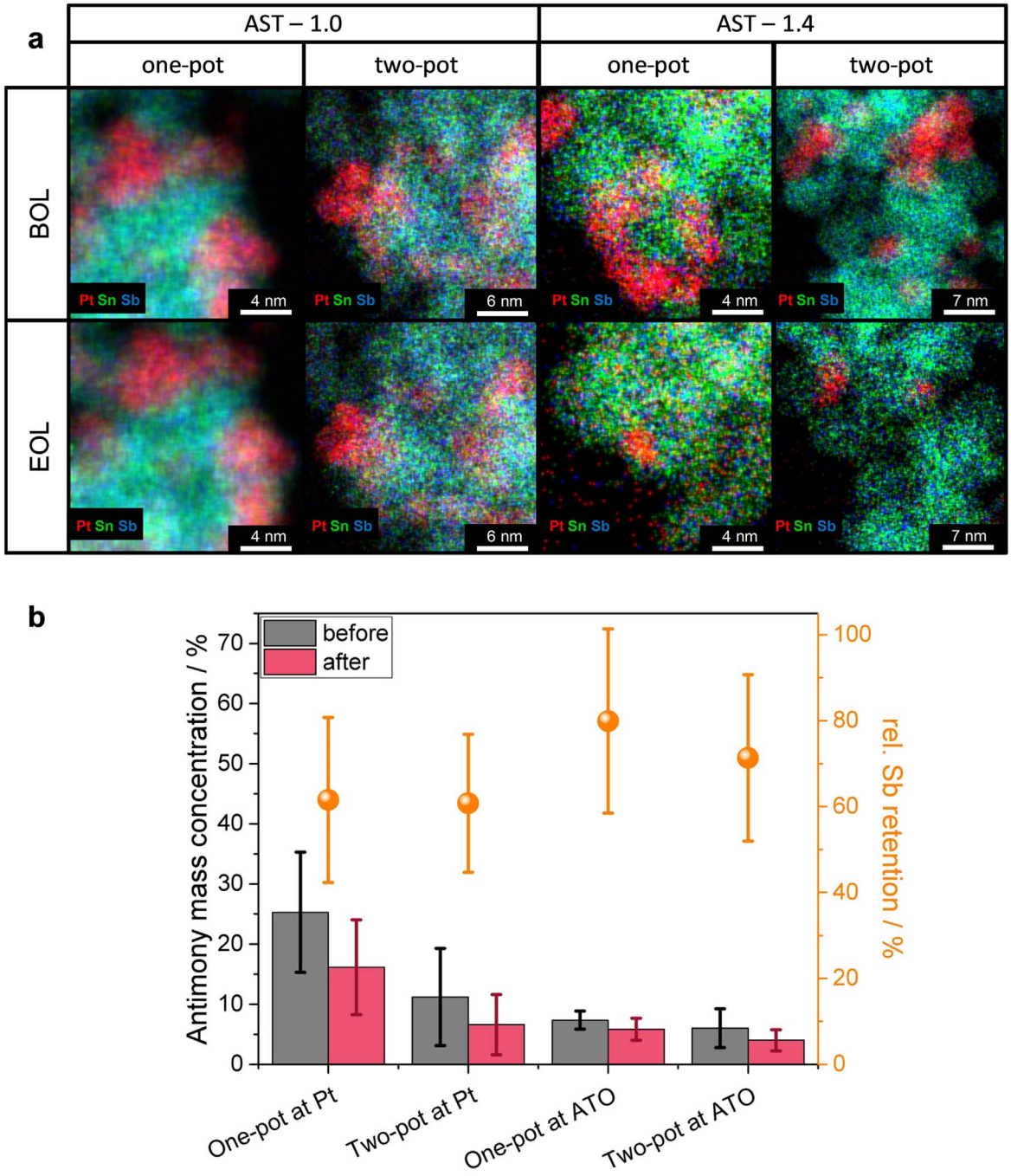

Figure 4. (a) IL-STEM experiments of Pt-11% Sb-ATO prepared with the one-pot and two-pot methods before (BOL) and after (EOL) AST-1.0 and AST-1.4. (b) Quantitative determination of the antimony concentrations before and after AST-1.0 by local mapping of the antimony concentration. Absolute average values of the antimony mass concentration given for positions with platinum particles and for the ATO support material. Relative antimony retention is given in orange dots. Errors are represented by the standard deviation.

influenced by the formation of the Pt-Sb alloy nor by the absolute increase in antimony amount in close proximity to platinum. After AST-1.4, however, nearly all platinum dissolves and its dissolution behavior is not affected by the respective support material. The loss of platinum particles additionally prevents the quantification of the antimony concentration after the stress test in an equal manner to the samples after AST-1.0.

Since the main advantage of the synthesized oxide supports lies in the reported wide operating potential window, the dissolution stability was analyzed via a scanning flow cell (SFC) coupled to an inductively coupled plasma mass spectrometer (ICP-MS). The instrumentation allows for in situ determination of time- and potential-dependent dissolution of platinum, tin and antimony. To correlate the applied potential with metal dissolution, two cyclic voltammetry (CV) scans at 5 $mV \cdot s^{-1}$ from 0.05 V_{RHE} and 1.5 V_{RHE} in 0.1 M $HClO_4$ were conducted on Pt-11% Sb-ATO (one-pot) and on Pt-HGS (Fig. 5). When brought in contact with the electrolyte, antimony, platinum and tin dissolve due to surface restructuring and reduction of surface oxides. The system stabilizes with time and the dissolution drops below the detection limit of the ICP-MS. Platinum shows the typical dissolution characteristics when oxidized (> ca. 1.1 V_{RHE}) and reduced (< ca. 0.8 V_{RHE}) which is line with literature.[49] A stabilizing effect of ATO on the dissolution behavior of platinum was not detected which is in line with IL-STEM

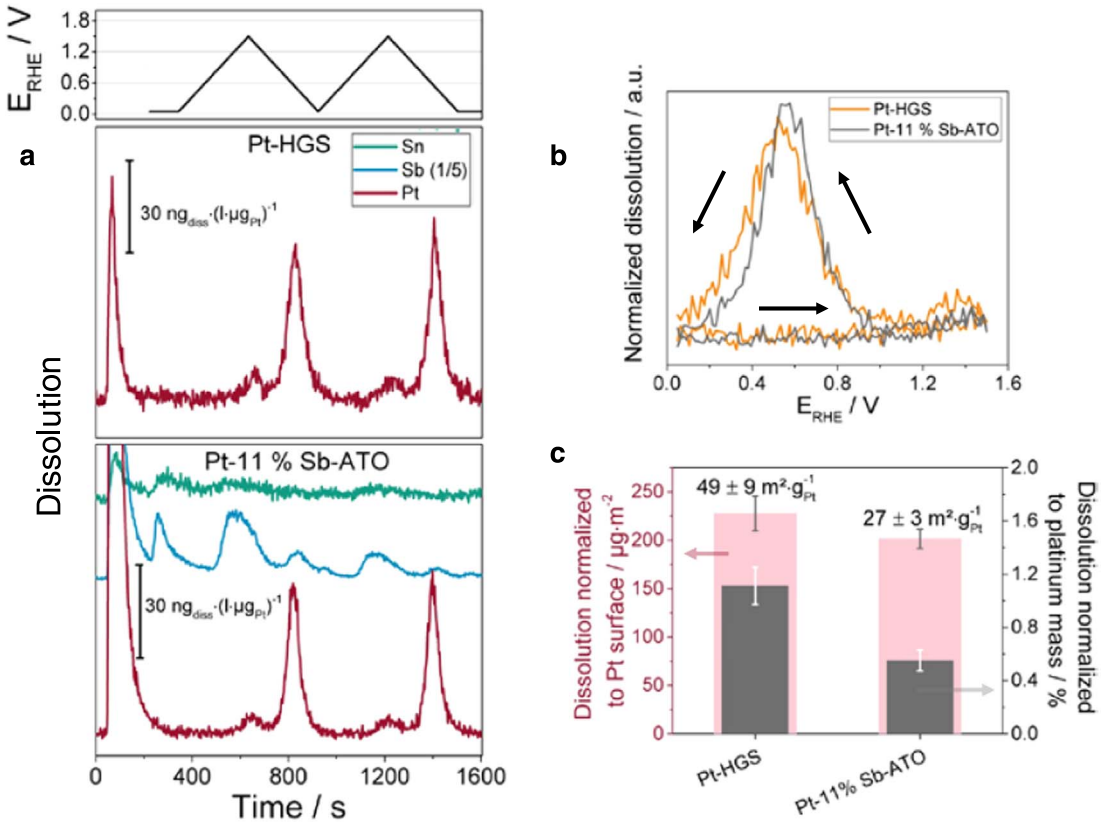

Figure 5. (a) Dissolution of antimony, tin and platinum during stability test (two CV 5 $mV \cdot s^{-1}$ from 0.05 V_{RHE} and 1.5 V_{RHE} in 0.1 M $HClO_4$) for Pt-HGS and Pt-11% Sb-ATO samples. Antimony dissolution for the latter sample was reduced by a factor of five. (b) Normalized dissolution (to the maximum value) vs potential graph from the first CV for the two samples shown in (a). (c) ECSA values determined by H_{UPD} and total Pt-dissolution during the electrochemical protocol normalized to the specific platinum surface (by H_{UPD}, left) and normalized to platinum mass (right). Data was compiled from four separate measurements. Platinum mass was determined from the dispersions by ICP-MS. The corresponding current-voltage diagram to (a) can be found in Fig. S13.

measurements. The total amount of platinum dissolved for ATO as support during cycling are comparable to Pt-HGS, if normalized to accessible platinum surface area. If normalized to the total platinum mass, the dissolution amounts are reduced, presumably caused by antimony/platinum interactions and antimony surface coverage, suppressing the transient oxidation and reduction of Pt. A previously reported transistor switching,[50] due to potential-dependent changes in conductivity, and the expected reduced platinum dissolution, was not observed. This might be caused by the generally low platinum dissolution in the potential range of ATO transistor switching.

For Sb, dissolution was observed at potentials below 0.3 V_{RHE}, which is triggered by the reduction of Sb-oxides.[24,51] Interestingly, for anodic antimony dissolution in the presence of platinum, the onset potential of antimony dissolution (0.6 V_{RHE}) is significantly reduced compared to pure ATO (1.1 V_{RHE},[24]). We hypothesize that OH*/O* adsorption on neighboring platinum atoms accelerates the re-oxidation of partly reduced Sb- to Sb(IV)-species that goes along with the observed dissolution.[40] During the cathodic scan, the onset of antimony dissolution is shifted to a more positive potential from 0.3 V_{RHE} for pure antimony to 0.8 V_{RHE} where reductive dissolution of platinum takes place (Fig. 5a). The high antimony dissolution rate has a drastic impact on the applicability in membrane electrode assemblies as described in detail in the SI. Significant antimony accumulation in the membrane, and antimony species permeating the membrane were observed after activity and degradation tests (Fig. S12).

Consequently, the stability window of antimony in ATO needs to be carefully adhered to in order to avoid mobilization of antimony by oxidation and reduction. Nevertheless, the best measure to reduce the amount of mobile species is to minimize the total antimony amount prone to mobilization. It has been shown that the concentration of weakly bound antimony surface species can be reduced by selecting an optimized antimony doping concentration as well as proper preparation and activation conditions.

Conclusions

In summary, we have provided an overview over platinum catalysts supported on various ATO materials and elaborated on their applicability regarding the oxygen reduction reaction. By altering the antimony concentration while keeping the Pt loading and Pt size, and overall support morphology the same, a detailed and fundamental understanding of the antimony influence on the catalytic performance of supported platinum catalysts was obtained. Our work demonstrates that antimony has a strong and overall negative impact on the ECSA and therefore performance of the platinum catalysts. The specific activity of Pt-ATO is at the same level compared to carbon supported Pt. The strong affinity of antimony to platinum, however, blocks catalytically active Pt-sites and results in a low overall performance. Antimony and platinum possess high affinity to each other and form agglomerates and alloys. The strong interaction is the main reason for the reduced mass activity and the decreased ECSA. Also obvious was the high mobility of antimony during electrochemical tests as both, the one- and two-pot synthesis result in similar ORR performances prior to and after AST-1.0 and AST-1.4. Due to the major impact of antimony on the catalyst and the membrane electrode assembly performance, the preparation of ATO support materials has to be optimized significantly to reduce the concentration of mobile antimony species; significant improvements might only be possible, if antimony leaching and mobilization can be prevented. However, as hitherto it appears that at the current stage of development Pt-ATO cannot compete with Pt-carbon in terms of mass activity.

Acknowledgments

We kindly acknowledge the contributions of S. Palm, A. Sold, H. Bongard for TEM and EDX measurements, J. Ternieden for valuable XRD measurements and A. Mingers (MPIE Düsseldorf) for support on ICP measurements. We thank C. Ochoa for important discussions. D. Jalalpoor acknowledges the International Max Planck Research School for Interface Controlled Materials for Energy Conversion (IMPRS-SurMat) for funding. ML acknowledge the Federal Ministry of Education and Research (BMBF) in the framework of NanoMatFutur (SynKat, FK: 03XP0265) for financial support. DG, VP, IR, KM, FS, PP, MH acknowledge the Federal Ministry for Economic Affairs and Energy (BMWi) of Germany in the framework of PtTM@HGS (project number 03ET6080A, 03ET6080B, 03ET6080C, 03ET6080D, 03ET6080E).

ORCID

Daniel Göhl https://orcid.org/0000-0003-3636-8870
Paul Paciok https://orcid.org/0000-0002-3432-3321
Marc Heggen https://orcid.org/0000-0002-2646-0078
Ivan Radev https://orcid.org/0000-0002-3895-6871
Karl J. J. Mayrhofer https://orcid.org/0000-0002-4248-0431
Marc Ledendecker https://orcid.org/0000-0003-3740-401X

References

1. M. Carmo, D. L. Fritz, J. Mergel, and D. Stolten, "A comprehensive review on PEM water electrolysis." *Int. J. Hydrogen Energy*, **38**, 4901 (2013).
2. J. K. Nørskov, J. Rossmeisl, A. Logadottir, L. Lindqvist, J. R. Kitchin, T. Bligaard, and H. Jónsson, "Origin of the overpotential for oxygen reduction at a fuel-cell cathode." *The Journal of Physical Chemistry B*, **108**, 17886 (2004).
3. E. Antolini, "Carbon supports for low-temperature fuel cell catalysts." *Appl. Catal. B-Environ.*, **88**, 1 (2009).
4. G. Polymeros et al., "High temperature stability study of carbon supported high surface area catalysts—expanding the boundaries of ex situ diagnostics." *Electrochim. Acta*, **211**, 744 (2016).
5. S. Sharma and B. G. Pollet, "Support materials for PEMFC and DMFC electrocatalysts-A review." *J. Power Sources*, **208**, 96 (2012).
6. Y. Y. Shao, J. Liu, Y. Wang, and Y. H. Lin, "Novel catalyst support materials for PEM fuel cells: current status and future prospects." *J. Mater. Chem.*, **19**, 46 (2009).
7. O. Lori and L. Elbaz, "Advances in ceramic supports for polymer electrolyte fuel cells." *Catalysts*, **5**, 1445 (2015).
8. E. Antolini and E. R. Gonzalez, "Ceramic materials as supports for low-temperature fuel cell catalysts." *Solid State Ionics*, **180**, 746 (2009).
9. D. Göhl, A. M. Mingers, S. Geiger, M. Schalenbach, S. Cherevko, J. Knossalla, D. Jalalpoor, F. Schüth, K. J. J. Mayrhofer, and M. Ledendecker, "Electrochemical stability of hexagonal tungsten carbide in the potential window of fuel cells and water electrolyzers investigated in a half-cell configuration." *Electrochim. Acta*, **270**, 70 (2018).
10. V. Muller, M. Rasp, G. Stefanic, J. H. Ba, S. Gunther, J. Rathousky, M. Niederberger, and D. Fattakhova-Rohlfing, "Highly conducting nanosized monodispersed antimony-doped tin oxide particles synthesized via nonaqueous sol-gel procedure." *Chem. Mater.*, **21**, 5229 (2009).
11. M. Dou, M. Hou, F. Wang, D. Liang, Q. Zhao, Z. Shao, and B. Yi, "Sb-doped SnO2 supported platinum catalyst with high stability for proton exchange membrane fuel cells." *J. Electrochem. Soc.*, **161**, F1231 (2014).
12. A. Fernandez-Vega, J. M. Feliu, A. Aldaz, and J. Clavilier, "Heterogeneous electrocatalysis on well defined platinum surfaces modified by controlled amounts of irreversibly adsorbed adatoms: Part II. Formic acid oxidation on the Pt (100)-Sb system." *J. Electroanal. Chem. Interfacial Electrochem.*, **258**, 101 (1989).
13. Y. Ogihara, H. Yano, M. Watanabe, A. Iiyama, and H. Uchida, "Effect of an Sb-doped SnO2 support on the CO-tolerance of Pt2Ru3 nanocatalysts for residential fuel cells." *Catalysts*, **6**, 139 (2016).
14. V. c. Climent, E. Herrero, and J. M. Feliu, "Electrocatalysis of formic acid and CO oxidation on antimony-modified Pt(111) electrodes." *Electrochim. Acta*, **44**, 1403 (1998).
15. G. Cognard, G. Ozouf, C. Beauger, G. Berthomé, D. Riassetto, L. Dubau, R. Chattot, M. Chatenet, and F. Maillard, "Benefits and limitations of Pt nanoparticles supported on highly porous antimony-doped tin dioxide aerogel as alternative cathode material for proton-exchange membrane fuel cells." *Appl. Catalysis B*, **201**, 381 (2017).
16. G. Ozouf and C. Beauger, "Niobium- and antimony-doped tin dioxide aerogels as new catalyst supports for PEM fuel cells." *J. Mater. Sci.*, **51**, 5305 (2016).
17. P. K. Mohanta, C. Glökler, A. O. Arenas, and L. Jörissen, "Sb doped SnO2 as a stable cathode catalyst support for low temperature polymer electrolyte membrane fuel cell." *Int. J. Hydrogen Energy*, **42**, 27950 (2017).
18. M. Yin, J. Xu, Q. Li, J. O. Jensen, Y. Huang, L. N. Cleemann, N. J. Bjerrum, and W. Xing, "Highly active and stable Pt electrocatalysts promoted by antimony-doped SnO2 supports for oxygen reduction reactions." *Appl. Catalysis B*, **144**, 112 (2014).
19. G. Cognard, G. Ozouf, C. Beauger, L. Dubau, M. López-Haro, M. Chatenet, and F. Maillard, "Insights into the stability of Pt nanoparticles supported on antimony-doped tin oxide in different potential ranges." *Electrochim. Acta*, **245**, 993 (2017).
20. S. Cavaliere, I. Jiménez-Morales, G. Ercolano, I. Savych, D. Jones, and J. Rozière, "Highly stable PEMFC electrodes based on electrospun antimony-doped SnO2." *ChemElectroChem*, **2**, 1966 (2015).
21. E. Fabbri, A. Rabis, Y. Chino, M. Uchida, and T. J. Schmidt, "Boosting Pt oxygen reduction reaction activity by tuning the tin oxide support." *Electrochem. Commun.*, **83**, 90 (2017).
22. J. C. Meier, C. Galeano, I. Katsounaros, J. Witte, H. J. Bongard, A. A. Topalov, C. Baldizzone, S. Mezzavilla, F. Schuth, and K. J. Mayrhofer, "Design criteria for stable Pt/C fuel cell catalysts." *Beilstein J. Nanotechnol.*, **5**, 44 (2014).
23. G. Ozouf, G. Cognard, F. Maillard, M. Chatenet, L. Guétaz, M. Heitzman, P. Jacques, and C. Beauger, "Sb-doped SnO_2 aerogels based catalysts for proton exchange membrane fuel cells: Pt deposition routes, electrocatalytic activity and durability." *J. Electrochem. Soc.*, **165**, F3036 (2018).
24. D. D. Jalalpoor, "Morphology controlled high-surface area support materials for electrochemical applications." (2019), https://hss-opus.ub.ruhr-uni-bochum.de/opus4/frontdoor/index/index/year/2019/docId/6241.
25. J. Knossalla, D. Jalalpoor, and F. Schüth, "Hands-on guide to the synthesis of mesoporous hollow graphitic spheres and core–shell materials." *Chem. Mater.*, **29**, 7062 (2017).
26. C. Galeano, J. C. Meier, V. Peinecke, H. Bongard, I. Katsounaros, A. A. Topalov, A. Lu, K. J. Mayrhofer, and F. Schuth, "Toward highly stable electrocatalysts via nanoparticle pore confinement." *J. Am. Chem. Soc.*, **134**, 20457 (2012).
27. TOPAS V5, *General Profile and Structure Analysis Software for Powder Diffraction Data. - User's Manual* (Bruker AXS, Karlsruhe, Germany) (2014).
28. G. J. McCarthy and J. M. Welton, "X-ray diffraction data for SnO2. an illustration of the new powder data evaluation methods." *Powder Diffr.*, **4**, 156 (1989).
29. S. United and H. E. Swanson, *Standard X-ray Diffraction Powder Patterns.* (U. S. Dept. of Commerce, National Bureau of Standards, Washington) 539 (1953).
30. K. J. J. Mayrhofer, D. Strmcnik, B. B. Blizanac, V. Stamenkovic, M. Arenz, and N. M. Markovic, "Measurement of oxygen reduction activities via the rotating disc electrode method: From Pt model surfaces to carbon-supported high surface area catalysts." *Electrochim. Acta*, **53**, 3181 (2008).
31. S. O. Klemm, A. A. Topalov, C. A. Laska, and K. J. J. Mayrhofer, "Coupling of a high throughput microelectrochemical cell with online multielemental trace analysis by ICP-MS." *Electrochem. Commun.*, **13**, 1533 (2011).
32. S. O. Klemm, A. Karschin, A. K. Schuppert, A. A. Topalov, A. M. Mingers, I. Katsounaros, and K. J. J. Mayrhofer, "Time and potential resolved dissolution analysis of rhodium using a microelectrochemical flow cell coupled to an ICP-MS." *J. Electroanal. Chem.*, **677–680**, 50 (2012).
33. J. Knossalla et al., "Shape-controlled nanoparticles in pore-confined space." *JACS*, **140**, 15684 (2018).
34. E. Pizzutilo et al., "The space confinement approach using hollow graphitic spheres to unveil activity and stability of Pt-Co nanocatalysts for PEMFC." *Adv. Energy Mater.*, **7**, 1700835 (2017).
35. R. Mohamed, T. Binninger, P. J. Kooyman, A. Hoell, E. Fabbri, A. Patru, A. Heinritz, T. J. Schmidt, and P. Levecque, "Facile deposition of Pt nanoparticles on Sb-doped SnO2 support with outstanding active surface area for the oxygen reduction reaction." *Catalysis Science & Technology*, **8**, 2672 (2018).
36. M. V. Maphoru, K. Pillai, and S. J. Heveling, "Structure-activity relationships of carbon-supported platinum-bismuth and platinum-antimony oxidation catalysts." *J. Catal.*, **348**, 47 (2017).
37. N. Kamiuchi, T. Matsui, R. Kikuchi, and K. Eguchi, "Nanoscopic observation of strong chemical interaction between Pt and Tin oxide." *The Journal of Physical Chemistry C*, **111**, 16470 (2007).
38. H. J. Goldschmidt and T. Land, "An X-ray investigation of the embrittlement of platinum and platinum-rhodium wires." *J. Iron Steel Inst.*, **155**, 221 (1947).
39. L. Hong and J. L.-C. Jiang Xiong, *Underpotential Deposition of Antimony(III) at a Platinum.*, **10**, 1049 (1994).
40. S. Geiger, O. Kasian, A. M. Mingers, K. J. J. Mayrhofer, and S. Cherevko, "Stability limits of tin-based electrocatalyst supports." *Sci. Rep.*, **7**, 4595 (2017).
41. E. Hornberger et al., "In situ stability studies of platinum nanoparticles supported on ruthenium−titanium mixed oxide (rto) for fuel cell cathodes." *ACS Catal.*, **8**, 9675 (2018).
42. C. S. Ko and R. J. Gorte, "Characterization of oxide impurities on Pt and their effect on the adsorption of CO and H2." *Surf. Sci.*, **155**, 296 (1985).
43. Q.-H. Wu, S.-G. Sun, X.-Y. Xiao, Y.-Y. Yang, and Z.-Y. Zhou, "An EQCM study of Sb adsorption and coadsorption with CO on Pt electrode in perchloric acid solutions." *Electrochim. Acta*, **45**, 3683 (2000).
44. D. F. van der Vliet, C. Wang, D. Li, A. P. Paulikas, J. Greeley, R. B. Rankin, D. Strmcnik, D. Tripkovic, N. M. Markovic, and V. R. Stamenkovic, *Unique Electrochemical Adsorption Properties of Pt-Skin Surfaces.*, **51**, 3139 (2012).
45. T. Binninger, E. Fabbri, R. Kötz, and T. J. Schmidt, "Determination of the electrochemically active surface area of metal-oxide supported platinum catalyst." *J. Electrochem. Soc.*, **161**, H121 (2014).
46. T. N. Geppert, M. Bosund, M. Putkonen, B. M. Stühmeier, A. T. Pasanen, P. Heikkilä, H. A. Gasteiger, and H. A. El-Sayed, "HOR activity of Pt-TiO2-Y at unconventionally high potentials explained: the influence of SMSI on the electrochemical behavior of Pt." *J. Electrochem. Soc.*, **167**, 084517 (2020).
47. C. A. Reiser, L. Bregoli, T. W. Patterson, J. S. Yi, J. D. Yang, M. L. Perry, and T. D. Jarvi, *A Reverse-Current Decay Mechanism for Fuel Cells.*, **8**, A273 (2005).

48. H. Tang, Z. Qi, M. Ramani, and J. F. Elter, "PEM fuel cell cathode carbon corrosion due to the formation of air/fuel boundary at the anode." *J. Power Sources*, **158**, 1306 (2006).
49. A. A. Topalov, S. Cherevko, A. R. Zeradjanin, J. C. Meier, I. Katsounaros, and K. J. J. Mayrhofer, "Towards a comprehensive understanding of platinum dissolution in acidic media." *Chem. Sci.*, **5**, 631 (2014).
50. T. Binninger, R. Mohamed, A. Patru, K. Waltar, E. Gericke, X. Tuaev, E. Fabbri, P. Levecque, A. Hoell, and T. J. Schmidt, "Stabilization of Pt nanoparticles due to electrochemical transistor switching of oxide support conductivity." *Chem. Mater.*, **29**, 2831 (2017).
51. M. Pourbaix, *Atlas of Electrochemical Equilibria in Aqueous Solutions.* (National Association of Corrosion Engineers, Houston, Texas, United States of America) (1974).